completely reversibly (compare the melting and freezing images at the same field). The inner solid islands, in contrast, are absent upon freezing, and then suddenly reappear at a lower field of 68.50 Oe. Once formed, the islands extend to their full size at the corresponding field, and proceed to behave reversibly as long as they are not fully melted again.

Reversible behaviour most probably reflects an equilibrium state of the system. The above results therefore imply that there is no supercooling or superheating when the solid–liquid interface is located in a region where the $H_m(x,y)$ landscape varies monotonically. The hysteretic behaviour occurs only when a new interface has to be formed, but only if this new interface surrounds a solid rather than a liquid. Hence, upon reducing H to below a local maximum of $H_m(x,y)$, the solid island is not readily formed (see lower panel of Fig. 2a). In this regime a unique situation occurs: metastable supercooled liquid domains, which are present instead of the 'missing' solid islands, coexist with the surrounding equilibrium liquid. Only when the supercooling becomes sufficiently large does sudden nucleation occur, upon which the solid abruptly occupies the entire volume of the supercooled domains. This non-equilibrium process is observed only at local maxima of $H_m(x,y)$. We would expect a symmetric non-equilibrium mechanism to be present at minima of $H_m(x,y)$, where superheated solid would transform hysteretically into a liquid droplet, but such hysteresis is not found. The asymmetry between the supercooling and superheating on a macroscopic scale is usually ascribed to the surface wetting process, which prevents solid superheating[14]. In our case mesoscopic vortex droplets are formed within a solid and therefore such an asymmetry should not be expected. Nevertheless, the tips of the vortices near the top and bottom surfaces of the crystal experience a reduced elastic confinement potential due to the absence of the lattice outside the sample. As a result, the vortex tips may undergo a pre-melting transition similar to the surface wetting in atomic solids, which may prevent the superheating of the vortex solid. In contrast to atoms, however, each vortex tip is attached to a solid vortex in the bulk, and therefore is restricted in space and may not exhibit liquid properties. □

Received 10 April; accepted 27 May 2000.

1. Imry, Y. & Wortis, M. Influence of quenched impurities on first-order phase transitions. *Phys. Rev. B* **19,** 3580–3585 (1980).
2. Blatter, G. *et al.* Vortices in high-temperature superconductors. *Rev. Mod. Phys.* **66,** 1125–1388 (1994).
3. Nelson, D. R. Vortex entanglement in high-T_c superconductors. *Phys. Rev. Lett.* **60,** 1973–1976 (1988).
4. Safar, H. *et al.* Experimental evidence for a first-order vortex-lattice-melting transition in untwinned single crystal $YBa_2Cu_3O_7$. *Phys. Rev. Lett.* **69,** 824–827 (1992).
5. Kwok, W. K. *et al.* Vortex lattice melting in untwinned and twinned single-crystals of $YBa_2Cu_3O_{7-\delta}$. *Phys. Rev. Lett.* **69,** 3370–3373 (1992).
6. Zeldov, E. *et al.* Thermodynamic observation of first-order vortex-lattice melting transition. *Nature* **375,** 373–376 (1995).
7. Zeldov, E. *et al.* Geometrical barriers in high-temperature superconductors. *Phys. Rev. Lett.* **73,** 1428–1431 (1994).
8. Indenbom, M. V. *et al.* Direct study of magnetic flux penetration and trapping in HTSC. *Physica C* **166,** 486–496 (1990).
9. Duran, C. A. *et al.* Real-time imaging of the magnetic flux distribution in superconducting $YBa_2Cu_3O_{7-\delta}$. *Nature* **357,** 474–477 (1992).
10. Welp, U. *et al.* Imaging of transport currents in superconducting $(Bi, Pb)_2SrCa_2Cu_3O_x$ composites. *Nature* **376,** 44–46 (1995).
11. Morozov, N. *et al.* Paramagnetic ac susceptibility at first-order vortex-lattice phase transition. *Phys. Rev. B* **54,** R3784–R3787 (1996).
12. Khaykovich, B. *et al.* Vortex-matter phase transitions in $Bi_2Sr_2CaCu_2O_8$: Effects of weak disorder. *Phys. Rev. B* **56,** R517–R520 (1997).
13. Oral, A. *et al.* Disorder-driven intermediate state in the lattice melting transition of $Bi_2Sr_2CaCu_2O_{8+\delta}$ single crystals. *Phys. Rev. B* **56,** R14295–14298 (1997).
14. Landau, L. D. & Lifshitz, E. M. *Statistical Physics* 3rd edn (Pergamon, Oxford, 1993).

Acknowledgements

We thank D. R. Nelson, Y. Imry, V. Vinokur, L. Balents, C. Varma, C. van der Beek and M. Indenbom for valuable discussions. This work was supported by the Israel Science Foundation and Center of Excellence Program, by the Ministry of Science, Israel, by the MINERVA Foundation, Munich, Germany, and by the Grant-in-Aid for Scientific Research from the Ministry of Education, Science, Sports and Culture, Japan.

Correspondence and requests for materials should be addressed to A. S. (email: hsasha@wisemail.weizmann.ac.il).

Optimal shapes of compact strings

Amos Maritan*, Cristian Micheletti*, Antonio Trovato* & Jayanth R. Banavar†

** International School for Advanced Studies (SISSA), Via Beirut 2–4, 34014 Trieste, Istituto Nazionale per la di Fisica della Materia (INFM) and the Abdus Salam International Center for Theoretical Physics, Trieste, Italy*
† Department of Physics and Center for Materials Physics, 104 Davey Laboratory, The Pennsylvania State University, University Park, Pennsylvania 16802, USA

Optimal geometrical arrangements, such as the stacking of atoms, are of relevance in diverse disciplines[1–5]. A classic problem is the determination of the optimal arrangement of spheres in three dimensions in order to achieve the highest packing fraction; only recently has it been proved[1,2] that the answer for infinite systems is a face-centred-cubic lattice. This simply stated problem has had a profound impact in many areas[3–5], ranging from the crystallization and melting of atomic systems, to optimal packing of objects and the sub-division of space. Here we study an analogous problem—that of determining the optimal shapes of closely packed compact strings. This problem is a mathematical idealization of situations commonly encountered in biology, chemistry and physics, involving the optimal structure of folded polymeric chains. We find that, in cases where boundary effects[6] are not dominant, helices with a particular pitch-radius ratio are selected. Interestingly, the same geometry is observed in helices in naturally occurring proteins.

The problem of placing spheres in three dimensions in order to attain the highest density was first posed by Kepler and has attracted much interest, culminating in its recent rigorous mathematical solution[1]. The close-packed hard-sphere problem may be restated in an alternative manner, more convenient for numerical implementation, as the determination of the arrangement of a set of points in a given volume that results in the minimum distance between any pair of points being as large as possible[6]. It is notable that the resulting 'bulk' optimal arrangement exhibits translational invariance in that, far from the boundaries, the local environment is the same for all points.

Here we introduce a new problem pertaining to the optimal shapes of compact strings. We consider a string (an open curve) in three dimensions. We use a geometric measure[7] of the curve, the 'rope length', defined as the arc length measured in units of the thickness, which has proved to be valuable in applications of knot theory[7–12]. The thickness Δ denotes the maximum radius of a uniform tube with the string passing through its axis, beyond which the tube either ceases to be smooth, owing to tight local bends, or it self-intersects. Our focus is on finding the optimal shape of a string of fixed arc length, subject to constraints of compactness, which would maximize its thickness, or equivalently minimize its rope length.

Following the approach of Gonzalez and Maddocks[10], who studied knotted strings, we define a global radius of curvature as follows. The global radius of curvature of the string at a given point is computed as the minimum radius of the circles going through that point and all other pairs of points of the string. It generalizes the concept of the local radius of curvature (the radius of the circle which locally best approximates the string) by taking into account both local (bending of the string) and non-local (proximity of another part of the string) effects. For discretized strings the local radius of curvature at a point is simply the radius of the circle going through the point and its two adjoining points. The minimum of all the global radii then defines the thickness, that is, the minimum radius of the circles going through any triplet of discrete points. This coincides with the previous definition in the continuum limit,

obtained on increasing the number of discretized points (assumed to be equally spaced) on the string while keeping the string length fixed[10].

We used several different boundary conditions to enforce the confinement of the string. The simplest ones discussed here are the confinement of a string of length l within a cube of side L or constraining it to have a radius of gyration (which is the r.m.s. distance of the discretized points from their centre of mass) that is less than a pre-assigned value R. Even though different boundary conditions influence the optimal string shape, the overall features are found to be robust. Examples of optimal shapes, obtained from numerical simulations, for different ratios of l/L and l/R are shown in Fig. 1. In both cases, two distinct families of strings, helices and saddles, appear. The two families are close competitors for optimality and different boundary conditions may stabilize one over the other. For example, if optimal strings of fixed length are constrained to have a radius of gyration less than R, then upon decreasing R, the string goes from a regime where the trivial linear string is curled into an arc, then into a portion of helix and finally into a saddle. When the string is constrained to lie within a cube of size L, as L decreases first saddles are observed and then helices.

We have also been able to find bulk-like solutions which are not influenced by boundary effects. Such solutions can be obtained by imposing uniform local constraints along the string. On imposing a minimum local density on successive segments of the string (for example, constraining each set of six consecutive beads to have a radius of gyration less than a preassigned value) we obtained perfectly helical strings, as in Fig. 2, confirming that this is the optimal arrangement. Note that, in close analogy with the sphere-packing problem, the optimal shape displays translational invariance along the chain. In all cases, the geometry of the chosen helix is such that there is an equality of the local radius of curvature (determined by the local bending of the string) and the radius that is associated with a suitable triplet of non-consecutive points lying in two successive turns of the helix. This is a feature that is observed only for a special ratio c^* of the pitch, p, and the radius, r, of the circle projected by the helix on a plane perpendicular to its axis. When $p/r > c^* = 2.512$ the global radius of curvature is equal to the local radius with the helix thickness given by $\Delta = r(1 + p^2/(2\pi r)^2)$. If $p/r < c^*$, the global radius of curvature is strictly lower than the local radius, and the helix thickness is determined basically by the distance between two consecutive helix turns: $\Delta \simeq p/2$ if $p/r \ll 1$. Optimal packing selects the very special helices corresponding to the transition between the two regimes described above. A visual example is provided by the optimal helix of Fig. 2.

For discrete strings, the critical ratio p/r depends on the discretization level. A more robust quantity is the ratio f, averaged over all the points of the string, of the minimum radius of the circles going through each point and any two non-adjacent points and the local radius. For discretized strings, $f = 1$ just at the transition described above, whereas $f > 1$ in the 'local' regime and $f < 1$ in the 'non-local' regime. In our computer-generated optimal strings, f differed from unity by less than one part in a thousand.

It is interesting to note that, in nature, there are many instances of the appearance of helices. For example, many biopolymers, such as proteins and enzymes, have backbones which frequently form helical motifs. (Rose and Seltzer[13] have used the local radii of curvature of the backbone as an input in an algorithm for finding the peptide chain turns in a globular protein.) It has been shown[14] that the emergence of such motifs in proteins (unlike in random heteropolymers which, in the melt, have structures conforming to gaussian statistics) is the result of the evolutionary pressure exerted by nature in the selection of native state structures that are able to

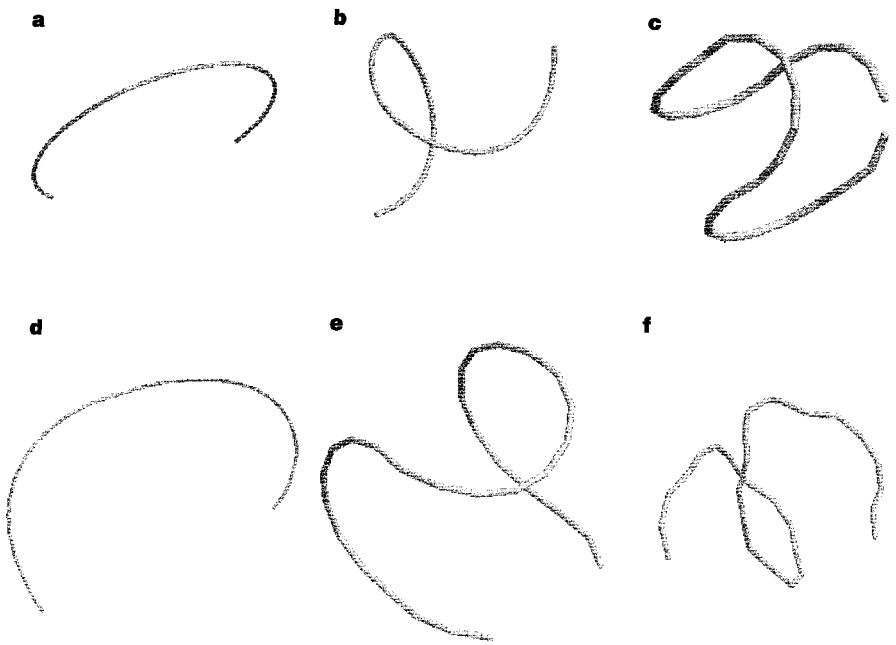

Figure 1 Examples of optimal strings. The strings in the figure were obtained starting from a random conformation of a chain made up of N equally spaced points (the spacing between neighbouring pints is defined to be 1 unit) and successively distorting the chain with pivot, crankshaft and slithering moves commonly used in stochastic chain dynamics[20]. A Metropolis Monte Carlo procedure is employed with a thermal weight, $e^{+\Delta/T}$, where Δ is the thickness and T is a fictitious temperature set initially to a high value such that the acceptance rate is close to 1 and then decreased gradually to zero in several thousand steps. Self-avoidance of the optimal string is a natural consequence of the maximization of the thickness. The introduction of a hard-core repulsion between beads was found to significantly speed up convergence to the optimal solution and avoid trapping in self-intersecting structures. We have verified that the same values (within 1%) of the final thickness of the optimal strings are obtained starting from unrelated initial conformations. **a**–**c**, Optimal shapes obtained by constraining strings of 30 points with a radius of gyration less than R. **a**, $R = 6.0$, $\Delta = 6.42$. **b**, $R = 4.5$, $\Delta = 3.82$. **c**, $R = 3.0$, $\Delta = 1.93$. **d**–**f**, Optimal shapes obtained by confining a string of 30 points within a cube of side L. **d**, $L = 22.0$, $\Delta = 6.11$. **e**, $L = 9.5$, $\Delta = 2.3$. **f**, $L = 8.1$, $\Delta = 1.75$.

house sequences of amino acids which fold reproducibly and rapidly[15] and are characterized by a high degree of thermodynamic stability[16]. Furthermore, because of the interaction of the amino acids with the solvent, globular proteins attain compact shapes in their folded states.

It is then natural to measure the shape of these helices and assess if they are optimal in the sense described here. The measure of f in α-helices found in naturally occurring proteins yields an average value for f of 1.03 ± 0.01, hinting that, despite the complex atomic chemistry associated with the hydrogen bond and the covalent bonds along the backbone, helices in proteins satisfy optimal packing constraints (for the measure of f we considered α-helices extracted from the unrelated proteins 1env, 1beo and 2end in the Protein Data Bank). This result implies that the backbone sites in protein helices have an associated free volume distributed more uniformly than in any other conformation with the same density. This is consistent with the observation[14] that secondary structures in natural proteins have a much larger configurational entropy than other compact conformations. This uniformity in the free volume distribution seems to be an essential feature because the requirement of a maximum packing of backbone sites by itself does not lead to secondary structure formation[15,19].Furthermore, the same result also holds for the helices appearing in the collagen native state structure, which have a rather different geometry (in terms of local turn angles, residues per turn and pitch[17]) from average α-helices. In spite of these differences, we again obtained an average $f = 1.01 \pm 0.03$ (Fig. 3), very close to the optimal value. □

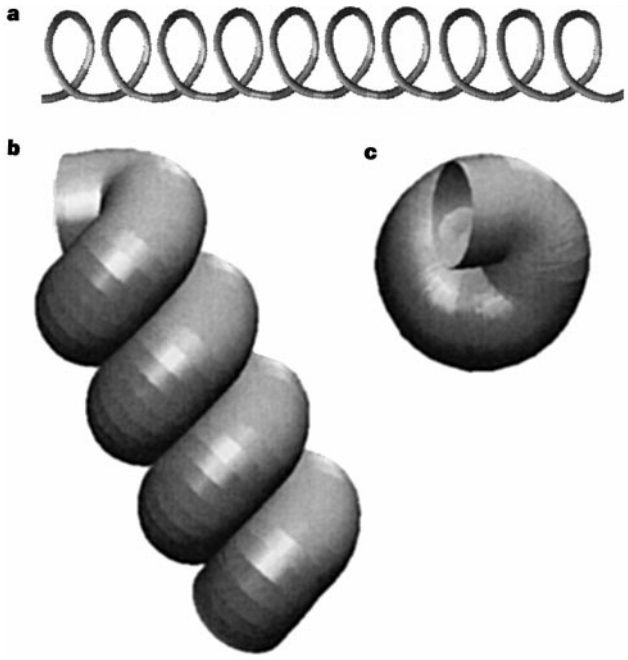

Figure 2 Optimal string with local constraint. The string has 65 points with a neighbour separation of unity. The local constraint was that each set of six consecutive beads had a radius of gyration less than 1. The value of f (see text for definition of the ratio) for this string is 0.9993. This result is quantitatively the same for a broad class of local constraints. **a**, The 'bare' skeleton of the optimal helix connecting the discrete beads. **b**, **c**, Side and top views of the same helix inflated to its thickness. Note that there is no free space either between consecutive turns of the helix or in the plane perpendicular to the helix axis.

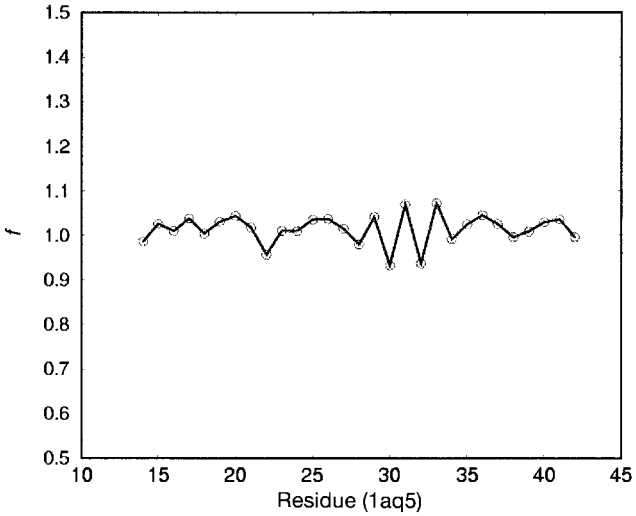

Figure 3 Packing of collagen helices. Plot of f values as a function of sequence position for a single collagen helix (only C_α coordinates were used to identify the protein backbone). The sample plot for each of the three collagen chains would simply superimpose. We considered the residues 14–41 from the structure 1aq5 in the Protein Data Bank.

1. Sloane, N. J. A. Kepler's conjecture confirmed. *Nature* **395,** 435–436 (1998).
2. Mackenzie, D. Mathematics—proving the perfection of the honeycomb. *Science* **285,** 1339–1340 (1999).
3. Woodcock, L. V. Entropy difference between the face-centred cubic and the hexagonal close-packed crystal structures. *Nature* **385,** 141–143 (1997).
4. Car, R. Crystal structure—how hard spheres stack up. *Nature* **385,** 115–116 (1997).
5. Cipra, B. Mathematics—packing challenge mastered at last. *Science* **281,** 1267 (1998).
6. Stewart, I. Tight tins for round sardines. *Sci. Am. Feb.* 80–82 (1998).
7. Buck, G. & Orloff, J. A simple energy function for knots. *Topol. Appl.* **61,** 205–214 (1995).
8. Katritch, V. *et al.* Geometry and physics of knots. *Nature* **384,** 142–145 (1996).
9. Katritch, V., Olson, W. K., Pieranski, P., Dubochet, J. & Stasiak, A. Properties of ideal composite knots. *Nature* **388,** 148–151 (1997).
10. Gonzalez, O. & Maddocks, J. H. Global curvature, thickness and the ideal shapes of knots. *Proc. Natl Acad. Sci. USA* **96,** 4769–4773 (1999).
11. Buck, G. Four thirds power law for knots and links. *Nature* **392,** 238–239 (1998).
12. Cantarella, J., Kusner, R. B. & Sullivan, J. M. Tight knot values deviate from linear relations. *Nature* **392,** 237–238 (1998).
13. Rose, G. D. & Seltzer, J. P. A new algorithm for finding the peptide chain turns in a globular protein. *J. Mol. Biol.* **113,** 153–164 (1977).
14. Micheletti, C., Maritan, A. & Banavar, J. R. Protein structures and optimal folding from a geometrical variational principle. *Phys. Rev. Lett.* **82,** 3372–3375 (1999).
15. Maritan, A., Micheletti, C. & Banavar, J. R. Role of secondary motifs in fast folding polymers: a dynamical variational principle. *Phys. Rev. Lett.* **84,** 3009–3012 (2000).
16. Sali, A., Shakhnovich, E. & Karplus, M. How does a protein fold? *Nature* **369,** 248–251 (1994).
17. Creighton, T. E. *Proteins—Structures and Molecular Properties* 182–188 (Freeman, New York, 1993).
18. Yee, D. P., Chan, H. S., Havel, T. F. & Dill, K. A. Does compactness induce secondary structure in proteins? Study of poly-alanine chains computed by distance geometry. *J. Mol. Biol.* **241,** 557–573 (1994).
19. Socci, N. D., Bialek, W. S. & Onuchic, J. N. Properties and origins of protein secondary structure. *Phys. Rev.* **49,** 3440–3443 (1994).
20. Sokal, A. D. Monte Carlo methods for the self-avoiding walk. *Nucl. Phys.* ***B47,*** 172–179 (1996).

Acknowledgements

This work was supported by INFN, NASA and The Donors of the Petroleum Research Fund administered by the American Chemical Society. A.T. thanks the Physics Department of Università degli Studi di Padova, Padova, Italy, for its hospitality.

Correspondence and requests for materials should be addressed to J.R.B. (e-mail: jayanth@phys.psu.edu).

Evidence for a link between global lightning activity and upper tropospheric water vapour

Colin Price

Department of Geophysics and Planetary Sciences, Tel Aviv University, Levanon Road, Ramat Aviv 69978, Israel

Tropospheric water vapour is a key element of the Earth's climate, which has direct effects as a greenhouse gas, as well as indirect effects through interaction with clouds, aerosols and tropospheric chemistry. Small changes in upper-tropospheric water vapour have a much larger impact on the greenhouse effect than small changes in water vapour in the lower atmosphere[1], but whether this impact is a positive or negative feedback remains uncertain[2–6]. The main challenge in addressing this question is the difficulty in monitoring upper-tropospheric water vapour globally over long timescales. Here I show that upper-tropospheric water-vapour variability and global lightning activity are closely linked, suggesting that upper-tropospheric water-vapour changes can be inferred from records of global lightning activity, readily obtained from observations at a single location on the Earth's surface. This correlation reflects the fact that continental deep-convective thunderstorms transport large amounts of water vapour into the upper troposphere and thereby dominate the variations of global upper-tropospheric water vapour while producing most of the lightning on Earth. As global lightning induces Schumann resonances, an electromagnetic phenomenon in the atmosphere that can be observed easily at low cost, monitoring of these resonances might provide a convenient method for tracking upper-tropospheric water-vapour variability and hence contribute to a better understanding of the processes affecting climate change.

Both climate models and observations support the idea that higher temperatures will increase the amount of upper-tropospheric water vapour (UTWV)[2–5]. Observations indicate that UTWV may already be increasing[7]. Although there are some claims to the contrary[6], there is little evidence to support the argument for the existence of a negative water-vapour feedback. Climate models predict water-vapour increases in the upper troposphere of approximately 10% for every 1 K increase in temperature in that layer. Some climate models predict UTWV to increase by 20% for every 1 K increase in surface temperatures[5]. This sensitivity is greater than that predicted by the Clausius–Clapeyron equation (6% per 1 K at 300 K) since UTWV is influenced not only by temperature, but also by transport from the lower atmosphere. Furthermore, while tropical surface temperatures may increase by 2–3 °C in a warmer climate, the upper tropical troposphere is expected to warm by 6–7 °C (ref. 1). As a result, the water-vapour feedback could amplify the surface temperature change due to a doubling of carbon dioxide by 60% (ref. 8).

UTWV is transported aloft by deep convection, later to be redistributed zonally and meridionally in the upper atmosphere[9]. A significant fraction of the water mass that is cycled through these clouds is transported as liquid droplets and ice particles. The stronger the updrafts, the deeper these cloud and precipitation particles are transported into the upper levels of clouds. Not only does the intensity of the convection influence the volume of water transported aloft, but it simultaneously influences the electrification processes in these convective clouds[10]. Radar studies of deep tropical convective storms show significant differences in the vertical structure of storms with large lightning activity relative to those storms that are weakly electrified[11]. In the case of storms with large lightning frequencies, the updrafts are strong enough to transport large amounts of supercooled droplets and graupel particles (soft hail) into the upper troposphere. The eventual sublimation of the large ice-filled anvil clouds results in a major source of water vapour into the upper troposphere[12,13]. It is possible that the precipitation and sublimation of large ice particles from these anvils will also moisten the mid-troposphere[14], while the advection of water vapour over the oceans[11] may result in the re-formation of new cirrus over the oceans[15]. Large amounts of subvisible cirrus occur near the tropical

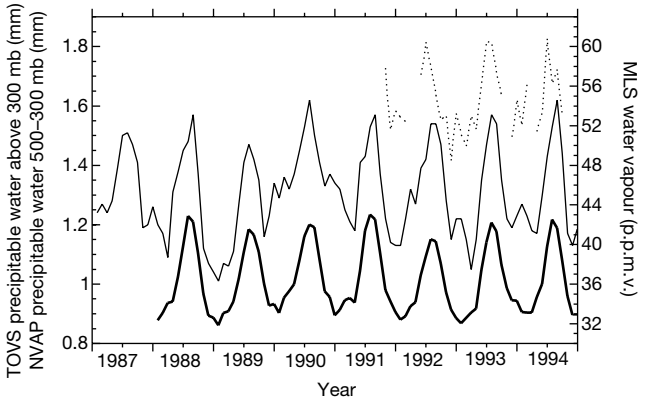

Figure 1 Seasonal variability of upper-tropospheric water vapour (UTVW). Monthly concentrations of water vapour at 215 mbar (MLS; dotted line), precipitable water above 300 mbar (TOVS; thin line) and precipitable water between 500–300 mbar (NVAP; thick line). The correlation between the NVAP and TOVS data sets (see text for description of data sets) is $r = 0.88$.